ORIGINAL ARTICLE

Journal
of the American Ceramic Society

Ultrasensitive optical thermometer based on abnormal thermal quenching Stark transitions operating beyond 1500 nm

Guotao Xiang[1] | Menglin Yang[1] | Qing Xia[1] | Sha Jiang[1] | Yongjie Wang[1] | Xianju Zhou[1] | Li Li[1] | Li Ma[2] | Xiaojun Wang[2] | Jiahua Zhang[3]

[1]Department of Mathematics and Physics, Chongqing University of Posts and Telecommunications, Chongqing, China

[2]Department of Physics & Astronomy, Georgia Southern University, Statesboro, GA, USA

[3]State Key Laboratory of Luminescence and Applications, Changchun Institute of Optics, Fine Mechanics and Physics, Chinese Academy of Sciences, Changchun, China

Correspondence

Dr. Guotao Xiang, Department of Mathematics and Physics, Chongqing University of Posts and Telecommunications, 2 Chongwen Road, Chongqing 400065, China.
Email: xianggt@cqupt.edu.cn

Dr. Xiaojun Wang, Department of Physics & Astronomy, Georgia Southern University, Statesboro, GA 30460, USA.
Email: xwang@georgiasouthern.edu

Dr. Jiahua Zhang, State Key Laboratory of Luminescence and Applications, Changchun Institute of Optics, Fine Mechanics and Physics, Chinese Academy of Sciences, 3888 Eastern South Lake Road, Changchun 130033, China.
Email: zhangjh@ciomp.ac.cn

Abstract

Light with wavelength longer than 1500 nm has great potential to afford deep bio-tissue penetration due to its extremely weak photon scattering and undetectable autofluorescence *in vivo*. Here, in order to satisfy the requirements for thermometry during the tumor hyperthermia process, an ultrasensitive optical thermometer operating beyond 1500 nm is developed by employing the thermally coupled Stark sublevels of Er^{3+}: $^4I_{13/2} \rightarrow {^4I_{15/2}}$ transition based on fluorescence intensity ratio (*FIR*) technology in Yb^{3+} and Er^{3+} codoped BaY_2O_4. Compared with the typical upconversion (UC) material β-$NaYF_4$: Yb^{3+}/Er^{3+} and Y_2O_3: Yb^{3+}/Er^{3+}, BaY_2O_4: Yb^{3+}/Er^{3+} shows more intense red Er^{3+}: $^4F_{9/2} \rightarrow {^4I_{15/2}}$ transition and 1.5 μm near-infrared (NIR) Er^{3+}: $^4I_{13/2} \rightarrow {^4I_{15/2}}$ transition induced by its larger phonon energy and higher quenching concentration of Er^{3+}. An equivalent four-level model is proposed to investigate the temperature characteristics of the NIR emission, from which four Stark transitions are separated from the raw spectra, named α, β, γ, and δ respectively. Then, the NIR thermal sensing performance have been developed by utilizing the *FIR* of I_β to I_α and I_γ to I_α. More importantly, an ultra-high sensitivity for optical thermometry has been obtained through the combination of transition β and γ, especially in the physiological temperature region. Furthermore, the detection depth of NIR light in bio-tissues is assessed by an *ex vivo* test, demonstrating that the maximal detection depth of NIR emission can reach to 8 mm without any influence on optical thermometry. These findings indicate that Yb^{3+} and Er^{3+} codoped BaY_2O_4 is a remarkable contender for optical thermometry in deep tissue with ultra-high sensitivity.

KEYWORDS
1.5 μm emission, energy transfer, Stark sublevel, temperature sensing, upconversion

1 | INTRODUCTION

Nowadays, cancer has become one of the major diseases leading to human death. However, the mainstream methods for cancer treatment such as surgery, chemotherapy, and radiotherapy used in the clinic reveal a lack of selectivity for cancer tissues and own serious side effects for human body. Therefore, massive effort have been made in the study of tumor hyperthermia, which can grasp the location of the lesion area and kill the cancer cells through hyperthermia focused ultrasound-based heating.[1] To ensure tumor cell carbonation and avoid damage to healthy tissues, a real-time noninvasive temperature monitor is very necessary.[2] At present, the major methods for temperature monitoring employed in tumor hyperthermia are Computed Tomography (CT), Thermal Microwave Radiation (TMR), and Magnetic Resonance Imaging (MRI).[3] However, serious X-ray radiation makes CT technology unsuitable for a long-time temperature measurement.[4] The penetration depth and temperature resolution of TMR technology in the bio-tissues failed to meet the requirements of tumor hyperthermia.[5] Temperature sensing based on MRI technology is characterized by high cost and excessive time delay.[6] Therefore, it is an urgent need to develop a novel temperature measurement method to satisfy the demand of tumor hyperthermia.

Non-invasive optical thermometry based on fluorescence intensity ratio (*FIR*) of thermally coupled energy levels (TCLs) of lanthanide ions in upconversion (UC) materials is a promising way to get over the above technical obstacle, due to the features of outstanding anti-jamming ability, excellent accuracy, and quick response capacity.[7–10] Meanwhile, UC materials own the advantages of high photostability and low toxicity, which makes them the promising candidates for monitoring the temperature *in vivo*.[11–16] However, the clinical performance of UC thermometers is far from satisfactory, which is severely hindered by the shallow penetration depth of the emitting visible light inside the organism resulting from the strong absorption and scattering by bio-tissues.[17] In order to address this problem, the UC sensors operating in the first (650–1000 nm, NIR-I) and second (1000–1700 nm, NIR-II) near-infrared (NIR) biological window have been widely developed, which are mainly based on the TCLs of Nd^{3+} under the excitation of 808 or 980 nm wavelength, such as $^4F_{5/2}/^4F_{3/2}$, $^4F_{7/2}/^4F_{3/2}$ and $^4F_{7/2}/^4F_{5/2}$.[18–22] However, the measurement deviation of Nd^{3+}-based thermometers would be much larger in practical application due to the serious overlap between the pumping laser band and the emission bands of Nd^{3+}.[23]

Actually, the long-wavelength NIR-II sub-window (1500–1700 nm, NIR-IIb) is better suited for bio-science than the NIR-I and short-wavelength NIR-II sub-window, which has been demonstrated by Dai et al. and Zhang et al. recently.[24,25] On the one hand, according to the Mie theory, the photons beyond 1500 nm own the weakest scattering phenomenon due to the inverse relationship between scattering coefficient and photon's wavelength.[26] On the other hand, the autofluorescence of the tissues caused by light emitting diode (LED) or laser excitation is undetectable beyond 1500 nm wavelength. The combination of negligible photon absorbance and scattering as well as the zero tissue-autofluorescence can significantly improve the penetration depth and signal-to-background ratio (SBR).[27] Even so, as far as we know, there is almost no relevant research on TCLs-based optical thermometer operating in NIR-IIb region (TOTN-IIb) to date.

Generally speaking, the separation ΔE between two TCLs used for optical thermometry should locate in the range of $200\ \text{cm}^{-1} \leq \Delta E \leq 2000\ \text{cm}^{-1}$ to avoid overlapping and decoupling.[28] Moreover, a great deal of research work has been done to improve the thermometric sensitivity by enlarging the ΔE value in the range mentioned above. However, the TCLs with large ΔE is ineffective for thermometry in physiological temperature region since relative strong heat activation is required to populate the upper thermal state from lower thermalized level, which has been proved by the recent publications.[29] For instance, Zhang et al. have reported that the thermally coupled Stark sublevels $^4F_{9/2(1)}/^4F_{9/2(2)}$ of Er^{3+} with a tiny $\Delta E \approx 190\ \text{cm}^{-1}$ possess a higher thermometric sensitivity than $^2H_{11/2}/^4S_{3/2}$ ($\Delta E \approx 780\ \text{cm}^{-1}$) in the physiological temperature range.[30] Similar conclusion has also been proposed by Guo's group.[31]

Er^{3+} is an especially distinguished activator for temperature sensing operating in visible range due to the remarkable thermal coupling property between $^2H_{11/2}$ state and $^4S_{3/2}$ state. Typically, under the assistance of Yb^{3+}, Er^{3+} can produce dazzling green or red light excited by 980 nm wavelength. Actually, an intense NIR emission band assigned to Er^{3+}: $^4I_{13/2} \rightarrow \ ^4I_{15/2}$ transition exists in the range from 1500 to 1600 nm concomitantly, which usually consists of several thermally coupled Stark splitting peaks with small ΔE caused by the crystal field effect. Therefore, the Stark sublevels of Er^{3+}: $^4I_{13/2} \rightarrow \ ^4I_{15/2}$ transition is an ideal candidate for TOTN-IIb.

In this study, BaY_2O_4 has been employed as a UC matrix for the first time. A dazzling red UC luminescence has been observed in BaY_2O_4: Yb^{3+}/Er^{3+} phosphor along with a strong $^4I_{13/2} \rightarrow \ ^4I_{15/2}$ transition in NIR region. The temperature sensing behaviors based on the *FIR* of the thermally coupled Stark sublevels of $^4I_{13/2} \rightarrow \ ^4I_{15/2}$ transition have been explored in detail. An equivalent four-level model is proposed to analyze the Stark splitting of $^4I_{13/2}$ and $^4I_{15/2}$ level, which gives rise to a significant improvement for the absolute sensitivity of the optical thermometer, especially in the physiological temperature region. The detection of the NIR light in bio-tissues can reach the depth of 8 mm without any affection on optical thermometry, which is demonstrated by an *ex vivo* experiment. The data show that BaY_2O_4: Yb^{3+}/Er^{3+} is a promising

material for temperature sensing in deep tissue, benefiting from the strong NIR emission beyond 1500 nm and ultra-high sensitivity within the physiological temperature range.

2 | EXPERIMENTAL PROCEDURE

2.1 | Preparation

The BaY_2O_4: y % Yb^{3+}/x % Er^{3+} powders is synthesized by a conventional solid state method with high temperature.[32–34] Firstly, weigh $BaCO_3$ (A.R.), Er_2O_3 (99.999%), Yb_2O_3 (99.999%), and Y_2O_3 (99.99%) in proportion and then mix them evenly in an agate mortar for sixty minutes. Finally, store the starting materials by an alumina crucible and sinter them in a box-type furnace with the temperature of 1300°C for 6 h.

2.2 | Characterization

A Persee XD-2 diffractometer is employed for the measurement of X-ray diffraction (XRD) data. A FLS920 spectrometer equipped with a 980 nm laser is used for the collection of luminescence spectra. The same spectrometer is utilized for the measurement of temperature dependent spectra equipped with a home-made electric furnace and *ex vivo* experiment.

## 3 | RESULTS AND DISCUSSION

3.1 | Crystal structure

Figure 1A,B depict the XRD patterns of the samples prepared by high temperature solid state method. Evidently, the positions and relative intensities of the diffraction peaks for the samples doped with various Yb^{3+} and Er^{3+} concentration match well with the standard XRD data of BaY_2O_4 (JCPDS 27–0044). No impure phase is detected, demonstrating a complete insertion for Yb^{3+} ions and Er^{3+} ions in BaY_2O_4 lattice have been realized. According to the previous paper published by Lopato's group, BaY_2O_4 owns an orthorhombic structure with a space group Pnma(62).[35] The lattice parameter of BaY_2O_4 is reported to be 1.0408, 0.3456, and 1.2126 nm for a, b, and c respectively. As displayed in Figure 1C, two different atom sites are occupied by Y (named Y1 and Y2) and only one type of atom site is occupied by Ba. The coordination numbers for Ba, Y1, and Y2 are eight, six, and six, respectively, as shown in Figure 1D.

3.2 | UC luminescence

The UC spectra of BaY_2O_4: y% Yb^{3+}/x% Er^{3+} are collected and presented in Figure 2A,B and Figure S1 and S2. Distinctly, the UC spectra are consisted of two weak green emission bands and a dominant red emission band, which are assigned to the Er^{3+}: $^2H_{11/2} \rightarrow {}^4I_{15/2}$ transition peaked at 523 nm, Er^{3+}: $^4S_{3/2} \rightarrow {}^4I_{15/2}$ transition peaked at 550 nm and Er^{3+}: $^4F_{9/2} \rightarrow {}^4I_{15/2}$ transition peaked at 663 nm respectively. It can be seen that the overall UC intensity is significantly enhanced by increasing Yb^{3+} or Er^{3+} concentration, resulting from the increasing number of the near-infrared (NIR) photons absorbed by Yb^{3+} or the luminescence centers Er^{3+}. Utilizing the variable-controlling approach, the optimal concentration of sensitizer Yb^{3+} and activator Er^{3+} for the strongest UC emission is confirmed to be 10% and 5% respectively. When Yb^{3+} or Er^{3+} doping concentration exceeds its corresponding optimal value, the UC intensity would be rapidly weakened caused by concentration quenching.

As is well known, β-$NaYF_4$ and Y_2O_3 are the most representative fluoride and oxide for UC luminescence respectively. Therefore, they are selected as the candidates for comparing the UC performance with BaY_2O_4. Figure 2C shows the UC spectra of BaY_2O_4: 10% Yb^{3+}/5% Er^{3+}, β-$NaYF_4$: 20% Yb^{3+}/2% Er^{3+}, and Y_2O_3: 10% Yb^{3+}/4%
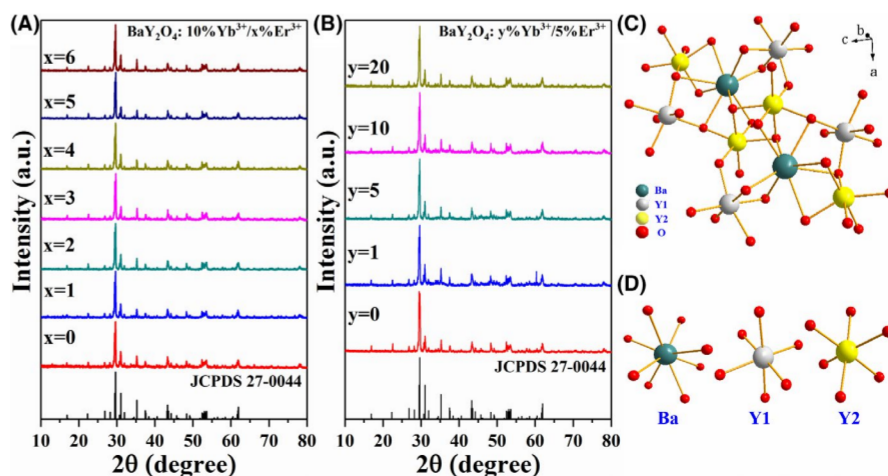
FIGURE 1 The XRD patterns of the samples doped with various (A) Er^{3+} concentration (x = 0, 1, 2, 3, 4, 5, 6) and (B) Yb^{3+} concentration (y = 0, 1, 5, 10, 20). (C) The crystal structure of BaY_2O_4. (D) The coordination environments of Ba and Y atom sites
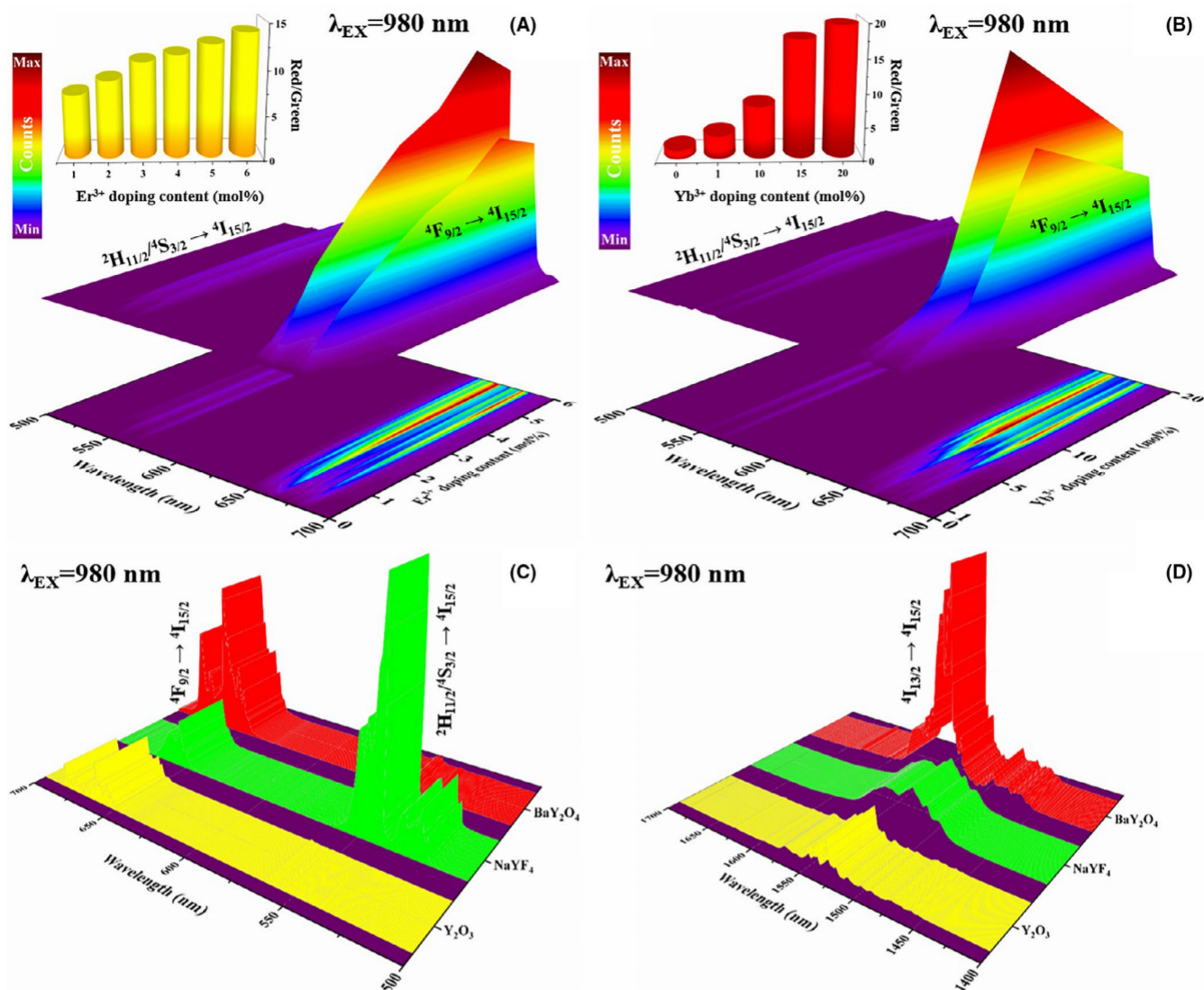
FIGURE 2 The visible spectra of the samples with different (A) Er^{3+} concentration and (B) Yb^{3+} concentration. The (C) UC and (D) NIR spectra of BaY_2O_4: 10% Yb^{3+}/5% Er^{3+}, β-$NaYF_4$: 20% Yb^{3+}/2% Er^{3+} and Y_2O_3: 10% Yb^{3+}/4% Er^{3+}. The inset of (A) and (B) shows the corresponding intensity ratio of red emission to green emission, respectively

Er^{3+}, which are measured under the same condition. The doping concentration of Yb^{3+} and Er^{3+} are the corresponding optimal values for every host. Obviously, β-$NaYF_4$: 20% Yb^{3+}/2% Er^{3+} owns the most intense green UC emission, but the strongest red UC emission belongs to BaY_2O_4: 10% Yb^{3+}/5% Er^{3+}. Through calculating the integral intensity of red UC, the emission intensity of BaY_2O_4: 10% Yb^{3+}/5% Er^{3+} is determined to be 4.1 times and 5.1 times stronger than that of β-$NaYF_4$: 20% Yb^{3+}/2% Er^{3+} and Y_2O_3: 10% Yb^{3+}/4% Er^{3+} respectively. Furthermore, the NIR spectra of the above three samples are also collected and displayed in Figure 2D. Evidently, a NIR emission band exists in all three samples, which originates from $^4I_{13/2} \rightarrow {}^4I_{15/2}$ transition of Er^{3+}. Similar to red UC emission, BaY_2O_4: 10% Yb^{3+}/5% Er^{3+} owns the strongest NIR emission, which is five times and seven times stronger than that of β-$NaYF_4$: 20% Yb^{3+}/2%

Er^{3+} and Y_2O_3: 10% Yb^{3+}/4% Er^{3+} respectively. As reported in our previous paper, in Yb^{3+}/Er^{3+} codoped system, the main populating route for Er^{3+}: $^4F_{9/2}$ level with red emitting is the energy transfer (ET) process from $^2F_{5/2}$ level of Yb^{3+} to $^4I_{13/2}$ of Er^{3+}.[36] Since the multiphonon relaxation (MPR) process from Er^{3+}: $^4I_{11/2}$ is dominant for populating Er^{3+}: $^4I_{13/2}$, it can be concluded that the intense red and NIR emission of BaY_2O_4: Yb^{3+}/Er^{3+} (~580 cm^{-1}) are mainly ascribed to its relatively larger phonon energy than that of β-$NaYF_4$: Yb^{3+}/Er^{3+} (~360 cm^{-1}) and Y_2O_3: Yb^{3+}/Er^{3+} (~460 cm^{-1}).[30,37,38] Beyond that, the matrix BaY_2O_4, β-$NaYF_4$ and Y_2O_3 own the same optimal molar concentration of Yb^{3+}, but the quenching concentration of Er^{3+} in BaY_2O_4 is higher than that in β-$NaYF_4$ and Y_2O_3, which is also beneficial for acquiring strong $^4F_{9/2} \rightarrow {}^4I_{15/2}$ transition and $^4I_{13/2} \rightarrow {}^4I_{15/2}$ transition of Er^{3+}. Concretely, as shown in the inset of Figure 2A,B,

the intensity ratio of red UC emission to green UC emission (R/G) is dramatically raised with the increasing Yb^{3+} or Er^{3+} doping concentration, indicating the appearance of a fast and efficient ET mechanism between the nearby Yb^{3+}-Er^{3+} pairs, which can result in the population of Er^{3+} $^4F_{9/2}$ state and the de-excitation of Er^{3+} $^4S_{3/2}$ state simultaneously.[13,31] As shown in Figure 3A, this process includes a cross relaxation (CR) ET process from Er^{3+} $^4S_{3/2}$ state to Yb^{3+} $^2F_{7/2}$ state (CR1) followed by a CR back (CRB) transfer process, taking place within the same Yb^{3+}-Er^{3+} pair. Moreover, at the high Er^{3+} doping concentration, a CR2 process between two neighboring Er^{3+} ions would appear, which also can enhance the red UC emission and weaken the green UC emission simultaneously, giving rise to the R/G improvement (see Figure 3A). It is thus evident that high-doping concentration of Yb^{3+} and Er^{3+} can facilitate the $^4F_{9/2} \rightarrow {}^4I_{15/2}$ transition and $^4I_{13/2} \rightarrow {}^4I_{15/2}$ transition of Er^{3+}. By virtue of the larger phonon energy and higher quenching concentration of Er^{3+}, BaY_2O_4: Yb^{3+}/Er^{3+} is suggested to be an excellent material for high efficient red UC emission and NIR emission beyond 1500 nm wavelength.
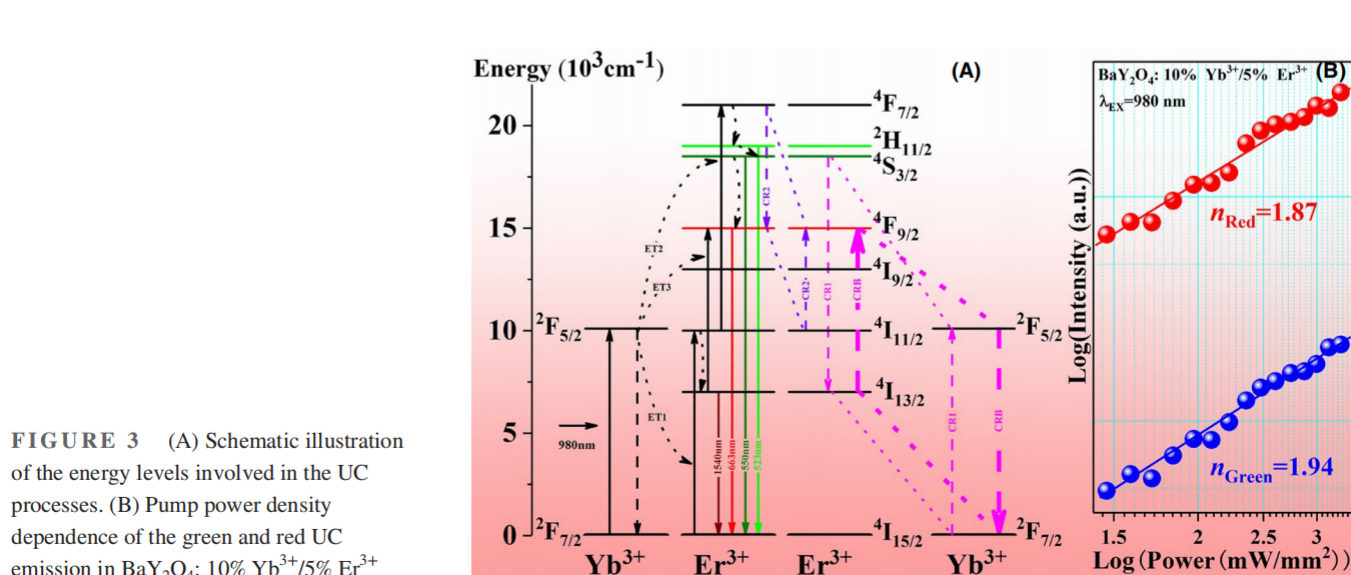
In order to clarify the UC mechanism in Yb^{3+} and Er^{3+} codoped BaY_2O_4, the excitation power density dependence of the UC emission is investigated. For the unsaturated UC process, the emission intensity I is proportional to P^n, namely $I \propto P^n$, where P denotes the power density of NIR laser and n represents the required number of NIR photons for emitting one visible photon. As shown in Figure 3B, the n value for green and red emission is 1.94 and 1.87, respectively, implying that two NIR photons are involved for producing one green or red photon.
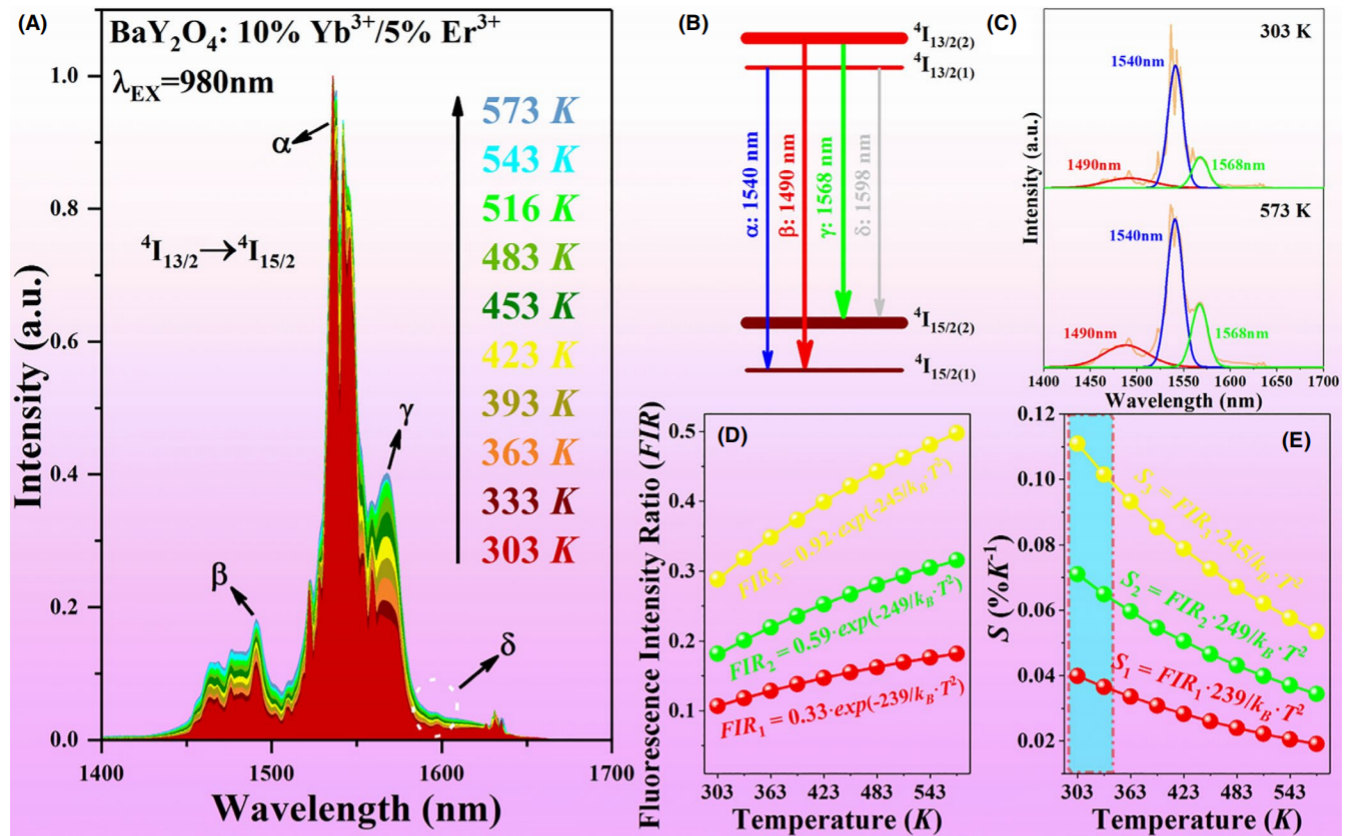
Based on the analysis mentioned above, the energy level diagram of Yb^{3+} and Er^{3+} and the possible ET processes are outlined and shown in Figure 3A. Exited by 980 nm wavelength, the NIR photons are mainly absorbed by Yb^{3+} ions due to the large absorption cross section at 980 nm, resulting

from the population of Yb^{3+}: $^2F_{5/2}$ state. Generally, the population for green emission states the $^2H_{11/2}$/$^4S_{3/2}$ of Er^{3+} are mainly derived from the MPR process of $^4F_{7/2}$ state, which is populated by the efficient ET1 process ($^2F_{5/2}$ (Yb^{3+}) + $^4I_{15/2}$ (Er^{3+}) → $^2F_{7/2}$ (Yb^{3+}) + $^4I_{11/2}$ (Er^{3+})) followed by the ET2 process ($^2F_{5/2}$ (Yb^{3+}) + $^4I_{11/2}$ (Er^{3+}) → $^2F_{7/2}$ (Yb^{3+}) + $^4F_{7/2}$ (Er^{3+})). Simultaneously, the excited Er^{3+} at the $^4I_{11/2}$ state can be de-excited to $^4I_{13/2}$ state through an MPR process and then receive energy from the excited Yb^{3+} (ET3), resulting in the population of red emission state $^4F_{9/2}$. Beyond that, the population of Er^{3+}: $^4F_{9/2}$ level can also be realized by the CR1-CRB process and CR2 process as well as the MPR process from $^2H_{11/2}$/$^4S_{3/2}$ state.

3.3 | Optical thermometry

Figure 4A shows the normalized NIR spectra of BaY_2O_4: 10% Yb^{3+}/5% Er^{3+} with various temperature. The power density of 980 nm laser is 1.4 mW/mm² to avoid the laser induced heating effect. Three distinct Stark transitions appear in the NIR emission band, named α at 1540 nm, β at 1490 nm, and γ at 1568 nm, respectively, deriving from the energy level splitting of $^4I_{13/2}$ and $^4I_{15/2}$. An equivalent four-level system is proposed to explore the temperature characteristics of Er^{3+}: $^4I_{13/2} \rightarrow {}^4I_{15/2}$ transition in detail. As shown in Figure 4B, both $^4I_{13/2}$ and $^4I_{15/2}$ multiplets are treated as a two-level system, including a lowest Stark sublevel and a group of higher Stark sublevels respectively. That is to say, except for the lowest Stark sublevel, the remaining Stark components are regarded as a whole. Thereby, in accordance with Boltzmann distribution law, the strongest emission α located at 1540 nm should belong to the transition from the lowest Stark sublevel of $^4I_{13/2}$ to the lowest Stark sublevel of $^4I_{15/2}$, namely $^4I_{13/2(1)} \rightarrow {}^4I_{15/2(1)}$.[39] Meanwhile, compared with transition α, the emission intensities of the

FIGURE 3 (A) Schematic illustration of the energy levels involved in the UC processes. (B) Pump power density dependence of the green and red UC emission in BaY_2O_4: 10% Yb^{3+}/5% Er^{3+}

FIGURE 4 (A) Normalized temperature dependent NIR spectra in BaY$_2$O$_4$: 10% Yb^{3+}/5% Er^{3+}. (B) An equivalent four-level system for depicting Er^{3+}: ^{4}I$_{13/2}$ → ^{4}I$_{15/2}$ transition. (C) The Lorentz fitting for Er^{3+}: ^{4}I$_{13/2}$ → ^{4}I$_{15/2}$ based on the equivalent four-level system. (D) The temperature dependence of (D) FIR and (E) S based on the Stark transition of Er^{3+}: ^{4}I$_{13/2}$ → ^{4}I$_{15/2}$

transition β at 1490 nm and γ at 1568 nm are obviously increased with the rising temperature, which results from the enhancement of the thermal population from ^{4}I$_{13/2(1)}$ to ^{4}I$_{13/2(2)}$, indicating that both β and γ originate from the higher Stark sublevel ^{4}I$_{13/2(2)}$. Finally, the wavelength of transition δ: ^{4}I$_{13/2(1)}$ → ^{4}I$_{15/2(2)}$ can be calculated by the following equation

$$\left| E_\alpha - E_\beta \right| = \left| E_\gamma - E_\delta \right|, \quad (1)$$

where E is the activation energy of the corresponding level. The calculated value reveals that the transition δ should locate at approximately 1600 nm. Coincidently, a very weak emission peak appears around 1598 nm as marked by a white cycle in Figure 4A, which is a potent evidence for the rationality of the equivalent four-level model. Sequentially, the NIR spectra of ^{4}I$_{13/2}$ → ^{4}I$_{15/2}$ transition are fitted by Lorentz functions referred to the equivalent four-level system, as shown in Figure 4C. Unfortunately, the emission band of transition δ failed to be separated from the raw spectra due to its extremely weak intensity, but this will not influence the following analysis.

Considering the thermal coupling between ^{4}I$_{13/2(1)}$ and ^{4}I$_{13/2(2)}$, the FIR_1 of I_β to I_α and FIR_2 of I_γ to I_α should be subject to the Boltzmann distribution law:

$$FIR_1 = I_\beta/I_\alpha = B_1 \bullet \exp\left(-\Delta E/k_B T\right). \quad (2)$$

$$FIR_2 = I_\gamma/I_\alpha = B_2 \bullet \exp\left(-\Delta E/k_B T\right). \quad (3)$$

Here, k_B, T, and I represent the Boltzmann constant, absolute temperature, and luminescence intensity respectively. ΔE is the energy gap between ^{4}I$_{13/2(1)}$ and ^{4}I$_{13/2(2)}$. B is a parameter ascertained by absorption rate, spontaneous emission, and degeneracy degree. Through a combination of Equation (2) and (3), then

$$FIR_3 = \left(I_\beta + I_\gamma\right)/I_\alpha = \left(B_1 + B_2\right)$$
$$\bullet \exp\left(-\Delta E/k_B T\right) = B_3 \bullet \exp\left(-\Delta E/k_B T\right), \quad (4)$$

where $(I_\beta + I_\gamma)$ is the whole emission intensity from ^{4}I$_{13/2(2)}$ sublevel. In this way, the fitting curves for the temperature dependence of FIR_1, FIR_2, and FIR_3 are achieved and presented in Figure 4D. The ΔE calculated by FIR_1, FIR_2, and FIR_3 are 239, 249, and 245 cm^{-1}, respectively, all close to the value of

218 cm^{-1} acquired from the NIR spectra. Meanwhile, all the three calculations through FIR_1, FIR_2, and FIR_3 result in very similar ΔE value, revealing the correctness of the equivalent four-level system once again. In order to take a quantitative assessment for the practicality of BaY_2O_4: Yb^{3+}/Er^{3+} as a temperature sensing probe, the values of the absolute sensitivity S are calculated by the following equation:

$$S = |d(FIR)/dT| = FIR \cdot (\Delta E/k_B T^2). \quad (5)$$

As plotted in Figure 4E, the absolute sensitivity S_1, S_2, and S_3 monotonously decrease with the increasing temperature and reach the maximum of 0.04, 0.07, and 0.11%K^{-1} at 303 K. Especially, thanks to the proportionality relationship between FIR and S, the absolute sensitivity of FIR_3 is much more
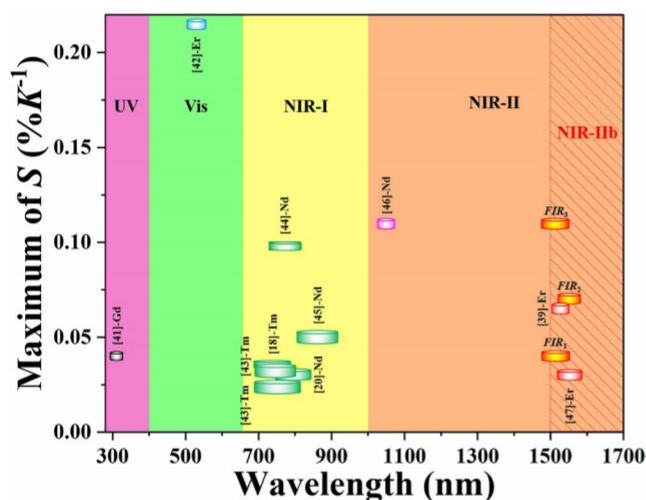

FIGURE 5 Comparison of the maximal S values between several typical FIR-based thermometers and the present sample

improved compared with that of FIR_1 and FIR_2 through the combination of transition β and γ.

Next, the thermometry performances of FIR_1, FIR_2, and FIR_3 in this work are further evaluated through a comprehensive comparison with other temperature sensors based on FIR technology. In order to take into account the effect of FIR value, the absolute sensitivity S is a better parameter to assess thermometry properties than the relative sensitivity $S_r = \Delta E/k_B T^2$.[40] As listed in Figure 5 and Table S1, the present BaY_2O_4: Yb^{3+}/Er^{3+} exhibits much larger sensitivity than the other Er^{3+}: $^4I_{13/2} \rightarrow {}^4I_{15/2}$ transition based optical thermometers reported previously, especially for FIR_3 thermometer.[39,47] Meanwhile, although the highest S value belongs to Er^{3+}: $^2H_{11/2}/^4S_{3/2} \rightarrow {}^4I_{15/2}$ transition based sensor working in the visible range, FIR_3 in this work owns the best performance for temperature measurement among the sensors working in the biological windows. What's more, the optimal working zone of FIR_3 perfectly locates in the physiological temperature region as depicted in Figure 4E. The above remarkable characteristics indicate the potential application of the present sample for optical thermometry *in vivo*.

Generally speaking, according to the Arrhenius law, the luminescence intensity of rare earth ions should be reduced at high temperature caused by the thermal quenching.[47–51] However, as shown in Figure S3, the absolute intensity of $^4I_{13/2} \rightarrow {}^4I_{15/2}$ transition is enhanced with the rising temperature, which is caused by the acceleration of the MPR process from $^4I_{11/2}$ level to $^4I_{13/2}$ level under high temperature.[52] The abnormal negative thermal quenching behavior of the $^4I_{13/2} \rightarrow {}^4I_{15/2}$ transition should benefit to further improve the SBR for temperature measurement in the bio-tissues. Besides that, the reproducibility study in the temperature circulation between 303 and 573 K for $^4I_{13/2} \rightarrow {}^4I_{15/2}$ transition is shown

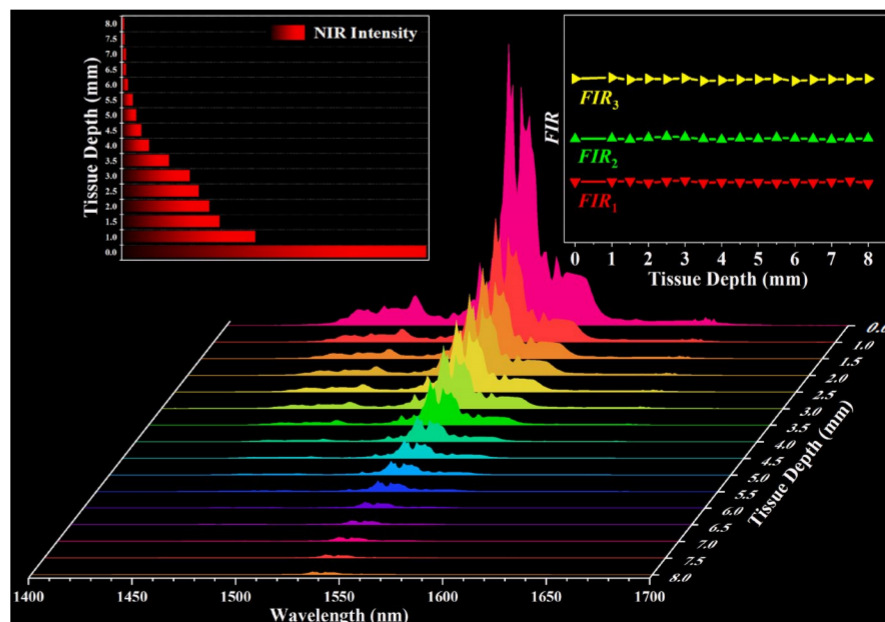**FIGURE 6** The NIR spectra and the corresponding integral intensities as well as the FIR values in BaY_2O_4: 10% $Yb^{3+}/5\%$ Er^{3+} excited by 980 nm wavelength with different thickness of chicken breast

in Figure S4. The values of FIR_1, FIR_2, and FIR_3 were almost unchanged upon in the circulation process, revealing their outstanding reproducibility.

3.4 | *Ex vivo* experiments in biological tissues

An *ex vivo* test is carried out with different thickness of chicken breast to evaluate the detection depth of NIR light beyond 1500 nm wavelength, which is a key value of temperature sensing for bio-science. As shown in Figure 6, the NIR emission of Er^{3+}: $^4I_{13/2} \rightarrow {}^4I_{15/2}$ transition is seriously decreased with the increasing tissue thickness. Even so, a clear spectroscopy signal can still be detected under 8-mm-thick tissue. Moreover, the values of FIR_1, FIR_2, and FIR_3 are seldom influenced by the increasing tissue thickness as depicted in the scatter plot graph, indicating their potential for a deep-tissue temperature sensing.

4 | CONCLUSIONS

In summary, an ultrasensitive optical thermometer BaY_2O_4: Yb^{3+}/Er^{3+} operating beyond 1500 nm wavelength is designed for tumor hyperthermia based on the FIR of Stark sublevels $^4I_{13/2(1)}$ and $^4I_{13/2(2)}$. The as-prepared sample shows much stronger $^4F_{9/2} \rightarrow {}^4I_{15/2}$ transition and $^4I_{13/2} \rightarrow {}^4I_{15/2}$ transition than the typical UC material β-$NaYF_4$: Yb^{3+}/Er^{3+} and Y_2O_3: Yb^{3+}/Er^{3+}, resulting from its larger phonon energy and higher quenching concentration of Er^{3+}. Based on an equivalent four-level model, it is proposed that transition α (1540 nm) and δ (1598 nm) originate from the lower Stark sublevel $^4I_{13/2(1)}$, and transition β (1490 nm) and γ (1568 nm) are ascribed to the upper Stark sublevel $^4I_{13/2(2)}$. Thereafter, the temperature sensing behaviors have been realized by utilizing the FIR_1 of $I_β$ to $I_α$ and FIR_2 of $I_γ$ to $I_α$ with the maximum S value of 0.04 and 0.07% K^{-1} at 303 K. More importantly, the absolute sensitivity is significantly improved by utilizing the FIR_3 of ($I_β + I_γ$) to $I_α$, resulting from the increasing FIR values. The optimal working zone of FIR_3 perfectly locates in the physiological temperature region with a maximum value of 0.11% K^{-1} at 303 K. Moreover, an abnormal negative thermal quenching behavior of the $^4I_{13/2} \rightarrow {}^4I_{15/2}$ transition has also been detected, benefitting to improve the SBR. In addition, the detection of the NIR light in bio-tissues can reach the depth of 8 mm without any influence on temperature sensing. All the findings declare that the present optical thermometer operating beyond 1500 nm wavelength with notably improved sensitivity is a promising phosphor for optical thermometry in the deep tissue during the tumor hyperthermia process.

ORCID

Guotao Xiang https://orcid.org/0000-0003-3587-6654
Sha Jiang https://orcid.org/0000-0001-7336-2115
Xianju Zhou https://orcid.org/0000-0003-0708-6081
Li Li https://orcid.org/0000-0003-1163-5733

REFERENCES

1. Tang R, Yu Q, Zhang K, Deng Q, Ma S, Li X. Clinical effect of intelligent temperature control system in preventing skin burns caused by tumor hyperthermia. J Med Imag Health In. 2020;10:1249–56.
2. Kickhefel A, Roland J, Weiss C, Schick F. Accuracy of real-time MR temperature mapping in the brain: a comparison of fast sequences. Phys Medica. 2010;26(4):192–201.
3. Nagarajan VK, Ward JM, Yu B. Association of liver tissue optical properties and thermal damage. Lasers Surg Med. 2020;52:779–87.
4. Fani F, Schena E, Saccomandi P, Silvestri S. CT-based thermometry: an overview. Int J Hyperther. 2014;30(4):219–27.
5. Spiliopoulos S, Theodosiadou V, Barampoutis N, Katsanos K, Davlouros P, Reppas L, et al. Multi-center feasibility study of microwave radiometry thermometry for non-invasive differential diagnosis of arterial disease in diabetic patients with suspected critical limb ischemia. J Diabetes Complicat. 2017;31(7):1109–14.
6. Odeen H, Parker DL. Improved MR thermometry for laser interstitial thermotherapy. Lasers Surg Med. 2019;51(3):286–300.
7. Zhang H, Zhao S, Wang X, Ren X, Ye J, Huang L, et al. The enhanced photoluminescence and temperature sensing performance in rare earth doped $SrMoO_4$ phosphors by aliovalent doping: from material design to device applications. J Mater Chem C. 2019;7(47):15007–13.
8. Xiang G, Liu X, Liu W, Wang B, Liu Z, Jiang S, et al. Multifunctional optical thermometry based on the stark sublevels of Er^{3+} in CaO-Y_2O_3: Yb^{3+}/Er^{3+}. J Am Ceram Soc. 2020;103(4):2540–7.
9. Gutierrez-Cano V, Rodriguez F, Gonzalez JA, Valiente R. Upconversion and Optical Nanothermometry in $LaGdO_3$: Er^{3+} Nanocrystals in the RT to 900 K Range. J Phys Chem C. 2019;123(49):29818–28.
10. Bastos ARN, Brites CDS, Rojas-Gutierrez PA, De Wolf C, Ferreira RAS, Capobianco JA, et al. Thermal properties of lipid bilayers determined using upconversion nanothermometry. Adv Funct Mater. 2019;29(48):1905474.
11. Dianov EM. Bismuth-doped optical fibers: a challenging active medium for near-IR lasers and optical amplifiers. Light: Sci Appl. 2012;1(3):e1.
12. Qin W-P, Liu Z-Y, Sin C-N, Wu C-F, Qin G-S, Chen Z, et al. Multi-ion cooperative processes in Yb^{3+} clusters. Light: Sci Appl. 2014;3(8):e193.
13. Zhang J, Hao Z, Li J, Zhang X, Luo Y, Pan G. Observation of efficient population of the red-emitting state from the green state

by non-multiphonon relaxation in the Er^{3+}-Yb^{3+} system. Light: Sci Appl. 2015;4(1):e239.

14. Liu K-C, Zhang Z-Y, Shan C-X, Feng Z-Q, Li J-S, Song C-L, et al. A flexible and superhydrophobic upconversion-luminescence membrane as an ultrasensitive fluorescence sensor for single droplet detection. Light: Sci Appl. 2016;5(8):e16136.

15. Wang F, Wen S, He H, Wang B, Zhou Z, Shimoni O, et al. Microscopic inspection and tracking of single upconversion nanoparticles in living cells. Light: Sci Appl. 2018;7(4):18007.

16. Liu W, Zhang Y, You W, Su J, Yu S, Dai T, et al. Near-infrared-excited upconversion photodynamic therapy of extensively drug-resistant *Acinetobacter baumannii* based on lanthanide nanoparticles. Nanoscale. 2020;12:13948–57.

17. Runowski M, Stopikowska N, Szeremeta D, Goderski S, Skwierczynska M, Lis S. Upconverting lanthanide fluoride core@shell nanorods for luminescent thermometry in the first and second biological windows: β-$NaYF_4$:Yb^{3+}-Er^{3+}@SiO_2 temperature sensor. ACS Appl Mater Interfaces. 2019;11(14):13389–96.

18. Suo H, Hu F, Zhao X, Zhang Z, Li T, Duan C, et al. All-in-one thermometer-heater up-converting platform YF_3: Yb^{3+}, Tm^{3+} operating in the first biological window. J Mater Chem C. 2017;5(6):1501–7.

19. Shou K, Qu C, Sun Y, Chen H, Chen S, Zhang L, et al. Multifunctional biomedical imaging in physiological and pathological conditions using a NIR-II probe. Adv Funct Mater. 2017;27(23):1700995.

20. Gao G, Busko D, Kauffmann-Weiss S, Turshatov A, Howard IA, Richards BS. Wide-range non-contact fluorescence intensity ratio thermometer based on Yb^{3+}/Nd^{3+} co-doped La_2O_3 microcrystals operating from 290 to 1230 K. J Mater Chem C. 2018;6(15):4163–70.

21. Xu W, Hu Y, Zheng L, Zhang Z, Cao W, Liu H, et al. Enhanced NIR-NIR luminescence from $CaWO_4$: Nd^{3+}/Yb^{3+} phosphors by Li^+ codoping for thermometry and optical heating. J Lumin. 2019;208:415–23.

22. Kolesnikov IE, Golyeva EV, Kalinichev AA, Kurochkin MA, Landeranta E, Mikhailov MD. Nd^{3+} single doped YVO_4 nanoparticles for sub-tissue heating and thermal sensing in the second biological window. Sensor Actuat B Chem. 2017;243:338–45.

23. Xu W, Zhao H, Zhang Z, Cao W. Highly sensitive optical thermometry through thermally enhanced near infrared emissions from Nd^{3+}/Yb^{3+} codoped oxyfluoride glass ceramic. Sensor Actuat B Chem. 2013;178:520–4.

24. Diao S, Blackburn JL, Hong G, Antaris AL, Chang J, Wu JZ, et al. Fluorescence Imaging In Vivo at Wavelengths beyond 1500 nm. Angew Chem Int Edit. 2015;54(49):14758–62.

25. Sun C, Li B, Zhao M, Wang S, Lei Z, Lu L, et al. J-aggregates of cyanine dye for NIR-II in vivo dynamic vascular imaging beyond 1500 nm. J Am Chem Soc. 2019;141(49):19221–5.

26. Bashkatov AN, Genina EA, Kochubey VI, Tuchin VV. Optical properties of human skin, subcutaneous and mucous tissues in the wavelength range from 400 to 2000 nm. J Phys D Appl Phys. 2005;38(15):2543–55.

27. Hong G, Antaris AL, Dai H. Near-infrared fluorophores for biomedical imaging. Nat Biomed Eng. 2017;1(1):1–22.

28. Demirkhanyan HG, Demirkhanyan GG, Kostanyan RB. YAG: Yb^{3+} crystal as a potential material for optical temperature sensors. Laser Phys. 2018;28(2):025701.

29. Shang Y, Han Q, Hao S, Chen T, Zhu Y, Wang Z, et al. Dual-mode upconversion nanoprobe enables broad-range thermometry from cryogenic to room temperature. ACS Appl Mater Interfaces. 2019;11(45):42455–61.

30. Wu H, Hao Z, Zhang L, Zhang X, Xiao Y, Pan GH, et al. Er^{3+}/Yb^{3+} codoped phosphor $Ba_3Y_4O_9$ with intense red upconversion emission and optical temperature sensing behavior. J Mater Chem C. 2018;6(13):3459–67.

31. Suo H, Guo C, Li T. Broad-scope thermometry based on dual-color modulation up-conversion phosphor $Ba_5Gd_8Zn_4O_{21}$:Er^{3+}/Yb^{3+}. J Phys Chem C. 2016;120(5):2914–24.

32. Li LI, Tang X, Wu Z, Zheng Y, Jiang S, Tang X, et al. Simultaneously tuning emission color and realizing optical thermometry via efficient $Tb^{3+} \rightarrow Eu^{3+}$ energy transfer in whitlockite-type phosphate multifunctional phosphors. J Alloy Compound. 2019;780:266–75.

33. Zhang J, Cai G, Wang W, Ma L, Wang X, Jin Z. Tuning of emission by Eu^{3+} concentration in a pyrophosphate: the effect of local symmetry. Inorg Chem. 2020;59(4):2241–7.

34. Wu ZC, Cui LL, Zhang X, Zhang XX, Liu J, Ma L, et al. Cationic substitution induced tuning of photoluminescence in $Ba_{2.94-2x}La_xNa_xP_4O_{13}$: 0.06 Eu phosphors for WLEDs. J. Alloy. Compound. 2020;835:155109.

35. Lopato L, Maister I, Shevchenko A. Physicochemical reactions of dysprosium, yttrium, and ytterbium oxider with barium oxide. Izv Akad Nauk SSSR Neorg Mater. 1972;8(5):861–4.

36. Xiang G, Zhang J, Hao Z, Zhang X, Luo Y, Lü S, et al. Transition to cubic phase and enhancement of green upconversion emission by adding La^{3+} ions in hexagonal $NaLuF_4$: Yb^{3+}/Er^{3+} nanocrystals. CrystEngComm. 2014;16(12):2499–507.

37. Xiang G, Zhang J, Hao Z, Zhang X, Pan GH, Luo Y, et al. Importance of suppression of Yb^{3+} de-excitation to upconversion enhancement in β-$NaYF_4$: Yb^{3+}/Er^{3+}@β-$NaYF_4$ sandwiched structure nanocrystals. Inorg Chem. 2015;54(8):3921–8.

38. Du P, Luo L, Yue Q, Li W. The simultaneous realization of high- and low-temperature thermometry in Er^{3+}/Yb^{3+}-codoped Y_2O_3 nanoparticles. Mater Lett. 2015;143:209–11.

39. Lei R, Liu X, Huang F, Deng D, Zhao S, Xu H, et al. Optical thermometry based on anomalous temperature-dependent 1.53 μm infrared luminescence of Er^{3+} in $BaMoO_4$: Er^{3+}/Yb^{3+} phosphor. Opt Mater. 2018;86:278–85.

40. Suo H, Zhao X, Zhang Z, Guo C. Ultra-sensitive optical nano-thermometer $LaPO_4$: Yb^{3+}/Nd^{3+} based on thermo-enhanced NIR-to-NIR emissions. Chem Eng J. 2020;389:124506.

41. Zheng K, Liu Z, Lv C, Qin W. Temperature sensor based on the UV upconversion luminescence of Gd^{3+} in Yb^{3+}-Tm^{3+}-Gd^{3+} codoped $NaLuF_4$ microcrystals. J Mater Chem C. 2013;1(35):5502–7.

42. Liu G, Sun Z, Fu Z, Ma L, Wang X. Temperature sensing and bio-imaging applications based on polyethylenimine/CaF_2 nanoparticles with upconversion fluorescence. Talanta. 2017;169:181–8.

43. Xing L, Yang W, Ma D, Wang R. Effect of crystallinity on the optical thermometry sensitivity of Tm^{3+}/Yb^{3+} codoped $LiNbO_3$ crystal. Sensor Actuat B Chem. 2015;221:458–62.

44. Tian X, Wei X, Chen Y, Duan C, Yin M. Temperature sensor based on ladder-level assisted thermal coupling and thermal-enhanced luminescence in $NaYF_4$: Nd^{3+}. Opt Express. 2014;22(24):30333–45.

45. Jiang G, Wei X, Zhou S, Chen Y, Duan C, Yin M. Neodymium doped lanthanum oxysulfide as optical temperature sensors. J Lumin. 2014;152:156–9.

46. Quintanilla M, Zhang Y, Liz-Marzan LM. Subtissue plasmonic heating monitored with CaF_2: Nd^{3+}, Y^{3+} nanothermometers in the second biological window. Chem Mater. 2018;30(8):2819–28.

47. Rakov N, Maciel GS. Exploring the $^4I_{13/2} \rightarrow {}^4I_{15/2}$ radiative transition from Er^{3+} in Y_2O_3 for temperature sensing. J Lumin. 2018;199:293–7.

48. Pattnaik S, Rai VK. Impact of charge compensation on optical and thermometric behaviour of titanate phosphors. Mater Res Bull. 2020;125:110761.

49. Feng Z, Lin L, Wang Z, Zheng Z. NIR optical temperature sensing with efficiently relative sensitivity based on β-$NaYF_4$: Er^{3+} nanoparticles. J Lumin. 2020;221:117005.

50. Du P, Luo L, Li W, Yue Q. Upconversion emission in Er-doped and Er/Yb-codoped ferroelectric $Na_{0.5}Bi_{0.5}TiO_3$ and its temperature sensing application. J Appl Phys. 2014;116:014102.

51. Du P, Luo L, Huang X, Yu J. Ultrafast synthesis of bifunctional Er^{3+}/Yb^{3+}-codoped $NaBiF_4$ upconverting nanoparticles for nanothermometer and optical heater. J Colloid Interf Sci. 2018;514:172–81.

52. Xiang G, Liu X, Zhang J, Liu Z, Liu W, Ma Y, et al. Dual-mode optical thermometry based on the fluorescence intensity ratio excited by a 915 nm wavelength in $LuVO_4$: Yb^{3+}/Er^{3+}@SiO_2 nanoparticles. Inorg Chem. 2019;58(12):8245–52.

SUPPORTING INFORMATION

Additional supporting information may be found online in the Supporting Information section.

How to cite this article: Xiang G, Yang M, Xia Q, Jiang S, Wang Y, Zhou X, et al. Ultrasensitive optical thermometer based on abnormal thermal quenching Stark transitions operating beyond 1500 nm. _J Am Ceram Soc_. 2021;00:1–10. https://doi.org/10.1111/jace.17981